Petroleum Science 23 (2026) 1428–1444

Contents lists available at ScienceDirect

Petroleum Science

journal homepage: www.keaipublishing.com/en/journals/petroleum-science

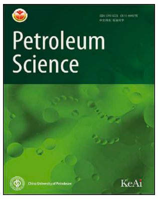

Original Paper

Dynamic evolution of residual oil during long-term waterflooding in Middle East carbonate reservoirs: A pore-scale investigation

Kai-Jun Tong [a], Yue Pan [b,c], Sheng Guo [a], Xiao-Cong Lyu [b,c,*], Han Chen [a], Hui-Qing Liu [b,c,**], Zhi-Xue Sun [d], Jia-Wei Tang [a]

[a] *CNOOC International Limited, Beijing, 100028, China*
[b] *State Key Laboratory of Petroleum Resources and Engineering, China University of Petroleum (Beijing), Beijing, 102249, China*
[c] *School of Petroleum Engineering, China University of Petroleum (Beijing), Beijing, 102249, China*
[d] *School of Petroleum Engineering, China University of Petroleum (East China), Qingdao, 266580, Shandong, China*

ARTICLE INFO

Article history:
Received 20 April 2025
Received in revised form
16 November 2025
Accepted 16 November 2025
Available online 20 November 2025

Edited by Yan-Hua Sun

Keywords:
Long-term water flooding (LTWF)
Microscopic pore-throat displacement characteristics
Residual oil dynamic evolution
Carbonate reservoir

ABSTRACT

Long-term water flooding (LTWF) is an efficient way to improve oil recovery (EOR) in carbonate reservoirs in the Middle East. Due to the complex depositional environment and intricate pore-throat structures of carbonate reservoirs, the development characteristics differ significantly from those of conventional sandstone reservoirs. While the mechanisms of LTWF in carbonate reservoirs are well-documented, there remains a significant gap in understanding the microscopic pore-scale displacement characteristics and the dynamic evolution of residual oil. To address this, nuclear magnetic resonance (NMR) and computed tomography (CT) scanning techniques were employed to investigate the behavior of LTWF across various carbonate rock samples. Initially, NMR technology was utilized to elucidate the pore-throat displacement characteristics at the microscopic level for different core samples under LTWF. Subsequently, CT scanning was applied to explore the dynamic evolution of microscopic residual oil and to categorize the types of residual oil based on their formation mechanisms. We found that LTWF predominantly utilizes oil within microscale pores of 1–10 μm and > 10 μm. As the volumes of injected water increase, there is a noticeable improvement in oil displacement within submicron pores (0.1–1 μm). However, residual oil primarily accumulates in nanopores (< 0.1 μm) and submicron pores. The study identified five distinct types of microscopic residual oil: clustered, throat, droplet, corner adsorbed, and pore lining. Notably, the transformation of residual oil in dolomite cores generally shifts from clustered to throat forms, while in limestone cores, it transitions from clustered to predominantly corner adsorbed and pore lining configurations. This nuanced understanding of oil utilization and residual categories under LTWF offers valuable insights into optimizing EOR strategies in complex carbonate reservoirs.

1. Introduction

Carbonate reservoirs are among the most significant oil and gas reservoirs globally, accounting for more than half of the world's remaining recoverable reserves. They represent a critical area for future oil and gas production growth. In the Middle East, the world's most resource-abundant region, approximately 80% of oil and gas production originates from carbonate reservoirs (Song and Li, 2018). The Asmari Formation, a Tertiary carbonate unit, serves as one of the region's most vital reservoir systems. The Asmari carbonate reservoirs are large, mixed-type systems characterized by diverse lithologies, including limestone, dolomite, mudstone, sandstone, and anhydrite (Khazaie et al., 2022; Sadeghi et al., 2011; Tong et al., 2024). These reservoirs exhibit complex structures, strong heterogeneity, and the development of multiple interbedded and barrier layers. Waterflooding remains a widely adopted EOR technique in Middle Eastern carbonate reservoirs. However, carbonate reservoirs possess intricate pore structures,

---

* Corresponding author.
** Corresponding author.
E-mail addresses: x.lyu@cup.edu.cn (X.-C. Lyu), liuhq@cup.edu.cn (H.-Q. Liu).

Peer review under the responsibility of China University of Petroleum (Beijing).

https://doi.org/10.1016/j.petsci.2025.11.031

including fractures and dissolution vugs, which exacerbate heterogeneity and complicate waterflooding dynamics (Sagbana et al., 2023; Song et al., 2018). The injected water tends to preferentially flow through fractures, leading to rapid water breakthrough and sharp declines in well productivity (Li et al., 2021; Tang et al., 2024). During long-term water flooding (LTWF), injected water primarily produces oil within larger pores, leaving oil in smaller pores unrecovered. This limitation often results in suboptimal waterflooding recovery efficiencies (Gong et al., 2024; Wang et al., 2021). It is therefore crucial to elucidate the microscopic displacement characteristics and the dynamic evolution of microscopic residual oil under LTWF in carbonate reservoirs. Gaining such insights is of significant importance for EOR in complex lithological carbonate reservoirs in the Middle East.

Currently, research on water flooding in carbonate reservoirs primarily focuses on three scales: microscopic, core, and reservoir (Bhicajee and Romero-Zerón, 2021; Chai et al., 2022; Mansi et al., 2020). At the microscopic scale, techniques such as CT scanning, NMR, and microfluidic chips are employed to directly observe and quantitatively analyze fluid distribution, migration, and trapping processes at the pore-throat level (Iraji et al., 2024; Jia et al., 2023; Liu et al., 2025). This is particularly valuable for carbonate reservoirs characterized by strong heterogeneity and multi-scale pore structures, as microscopic studies can effectively differentiate displacement behavior of water in various types of pore spaces. However, microscopic experiments are generally limited to millimeter- or centimeter-sized rock fragments, and a single small sample cannot capture the heterogeneity of an entire reservoir—or even a full core. Moreover, such experiments are typically conducted under conditions far removed from actual reservoir temperature and pressure, rendering their conclusions highly localized and lacking representativeness. At the core scale, core experiments serve as a crucial bridge linking microscopic mechanisms to reservoir engineering. Core-scale studies typically involve laboratory waterflooding tests on full-diameter cores or standard plug samples, complemented by the measurement of key petrophysical parameters such as relative permeability and capillary pressure curves (Darvish et al., 2019; Snosy et al., 2022). The major advantage of core-scale studies lies in their ability to simulate small-scale displacement processes under conditions approximating those in the reservoir, providing results of direct engineering relevance. Nevertheless, core-scale studies also suffer from fundamental limitations in representativeness. The pronounced heterogeneity of carbonate rocks implies that one or several cores cannot adequately represent the entire reservoir. Additionally, conventional core dimensions are insufficient to capture meaningful fracture or vug systems. Finally, at the reservoir scale, field-scale numerical simulation is a central technology for optimizing development strategies, reducing operational risks, and improving recovery efficiency. Its key value lies in integrating geological, fluid, and engineering data through digital modeling to enable dynamic forecasting and decision-making for complex reservoir systems (Li et al., 2022; Yang et al., 2022). However, reservoir-scale simulation is inherently constrained by its heavy reliance on input data quality and model simplifications, leading to significant uncertainties in prediction. For example, the intense heterogeneity of carbonate reservoirs is difficult to quantify accurately, and discrete fracture network models often rely on statistical assumptions that fail to reproduce the true complexity of fracture topology. Furthermore, multiphase flow equations frequently oversimplify microscale processes, neglecting pore-throat-level capillarity and the coupling between porous-media flow and free-flow regimes, which can result in substantial deviations in displacement efficiency predictions. In summary, there is an urgent need to develop an evaluation framework specifically tailored for water flooding in carbonate reservoirs, one that can partially bridge the gaps and limitations inherent to individual experimental scales.

In the petroleum industry, NMR and CT scanning technologies have been widely applied to sandstone reservoirs, enabling quantitative characterization of pore-throat structures, fluid distributions, and fluid displacement characteristics (Gong and Liu, 2020; Liu et al., 2017; She et al., 2021). However, carbonate reservoirs exhibit significantly stronger heterogeneity and more complex pore structures than sandstones, posing substantial challenges for the application of NMR in such systems. For instance, understanding the evolution of porosity and permeability in carbonates under long-term flow conditions remains a critical and challenging issue in petroleum engineering. To address this, Wang et al. (2023) employed NMR T_2 spectrum inversion combined with permeability measurements to quantitatively characterize changes in multi-scale pore volumes, revealing the competing mechanisms of stress-induced compaction and mineral dissolution during long-term infiltration. Their findings provide a theoretical basis for accurately predicting flow properties in carbonate reservoirs. The principal advantage of NMR lies in its ability to quantitatively evaluate fluid mobilization within pores of different scales. However, this requires converting the transverse relaxation time (T_2) spectrum into a pore-throat size distribution. In sandstone reservoirs, this conversion can be effectively achieved using classical models such as Schlumberger Doll Research or Coates models, which yield high fitting accuracy. In contrast, these conventional models perform poorly when applied to highly heterogeneous carbonates with intricate pore systems. In CT-based studies, researchers exploit differences in X-ray attenuation among materials and employ advanced image-processing algorithms to reconstruct digital cores. These digital cores facilitate quantitative analysis of pore-throat characteristics and allow for the spatial quantification of fluid distributions (McLendon et al., 2014). Moreover, they can be integrated with numerical simulations to model flow behavior at the core scale (Li et al., 2018). The main challenge in applying CT technology to carbonate reservoirs lies in accurately representing their highly complex multi-scale pore networks and connectivity, which are profoundly influenced by heterogeneity. Acid fracturing is a widely used technique to enhance recovery in carbonate reservoirs, but its effectiveness is often impacted by the presence of heterogeneous fractures and vugs. Han et al. (2025) utilized CT imaging to investigate fracturing behavior under various fluid types and injection strategies, clarifying fracture morphologies and dissolution patterns under acidizing conditions. Over the past decade, extensive research employing CT technology has been conducted on the microscopic distribution of residual oil in sandstone reservoirs. However, studies focusing on microscopic residual oil in carbonate reservoirs—particularly in the complex carbonate formations of the Middle East—remain relatively limited.

In this study, LTWF experiments were conducted on dolomite and limestone cores from the A oilfield in Iraq. First, NMR technology was utilized to characterize the microscopic pore-throat utilization under LTWF at the pore scale. This was achieved by establishing a nonlinear correlation between HPMI curves and NMR T_2 spectra for coordinate transformation. Subsequently, CT scanning technology was employed to reconstruct three-dimensional digital rock models by applying non-local mean filtering and threshold segmentation to CT scan data. This approach enabled the analysis of the dynamic evolution of microscopic residual oil under LTWF for different rock types. Furthermore, based on the formation mechanisms and spatial distribution characteristics of residual oil, five distinct types of residual oil were classified using three key parameters: shape factor, Euler number, and contact ratio. Ultimately, the findings of this study provide theoretical guidance for optimizing development strategies and enhancing oil recovery in the complex lithological carbonate reservoirs of the Middle East after LTWF.

2. Geological background

The Middle East is the most resource-rich region globally, with approximately 80% of its oil and gas production derived from carbonate reservoirs. Among these, the Tertiary Asmari Formation is a critical reservoir unit. In southeastern Iraq, the A oilfield is a giant oilfield with recoverable reserves exceeding hundreds of millions of tons, where the Asmari Formation serves as the primary productive reservoir. Located in Maysan Province, southeastern Iraq, near the Iranian border and approximately 175 km from Basra, the A oilfield lies on the southern margin of the Zagros foreland fold belt, adjacent to the Mesopotamian Basin (Fig. 1). The field exhibits a northwest-southeast elongated compressional anticline structure, formed under the significant northeast-southwest horizontal compressive stress generated by the Zagros orogeny (Jafari et al., 2020). The Asmari Formation in the A oilfield is a large mixed carbonate reservoir characterized by diverse lithologies, including limestone, dolomite, mudstone, and sandstone. The reservoir exhibits complex structures, strong heterogeneity, and features faults and fractures controlled by tectonics. Based on lithological assemblages and depositional characteristics, the Asmari Formation is divided into four members: A, B, C, and D. Members A and B are the main oil-bearing layers and the primary targets for current field development and this study (Joudaki and Baghbani, 2018). Members C and D are primarily water-bearing layers, which most development wells have not penetrated. Carbonate rocks predominantly occur in members A and B. Member A represents a restricted platform environment with dolomite as the main lithology, including bioclastic dolomite, oolitic dolomite, intraclast dolomite, and microcrystalline dolomite. Member B reflects a semi-restricted platform environment, with limestone as the dominant lithology, including bioclastic limestone, intraclast limestone, and micritic limestone.

3. Experimental setup and procedure

3.1. Experimental materials

3.1.1. Core samples

Four matrix-type carbonate rock cores were extracted from the Asmari Formation in the A oilfield, Iraq, comprising two dolomite samples from member A and two limestone samples from member B. According to image logging interpretation of the target reservoir, structural fractures are the dominant fracture type in the A oilfield. Core observations indicate that these structural fractures are primarily shear fractures with relatively stable and straight fracture surfaces. Based on the fracture characteristics of the reservoir, two types of cores were designed for the experiment: matrix-type cores and high-angle fractured cores. The high-angle fractured cores were created by cutting artificial fractures into matrix-type cores. The NMR experiments were conducted on standard cylindrical cores with a diameter of 25 mm and a length of 50 mm. To enhance the observation of residual oil distribution changes, the cores for CT scanning experiments were cut from the standard cores into smaller samples with a diameter of 5 mm and a

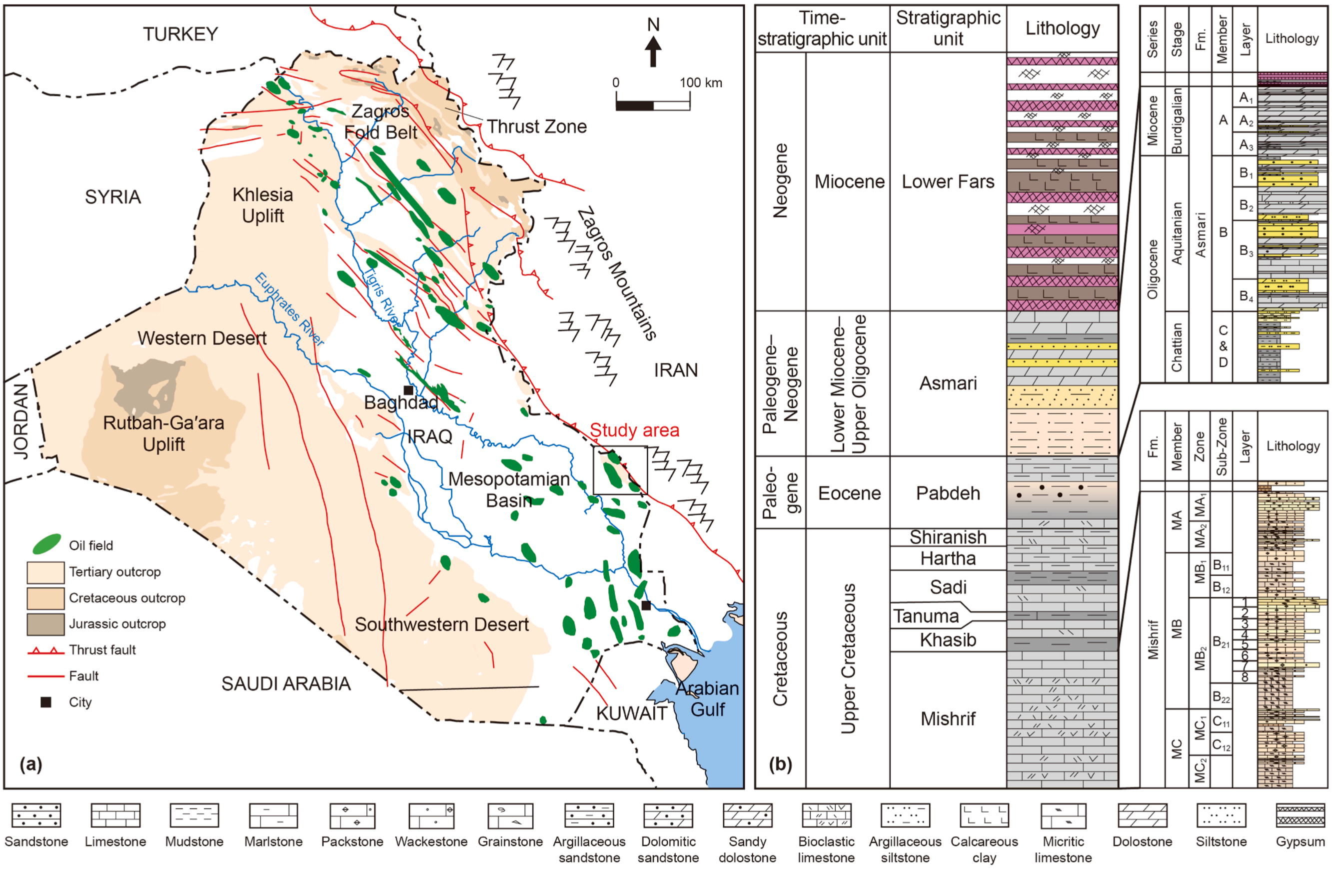

Fig. 1. A oilfield geological map. (**a**) Regional location map; (**b**) comprehensive column of Asmari Formation in the A oilfield, Iraq.

length of 10 mm. In this study, permeability and porosity measurements were performed using the standard cores (25 mm in diameter, 50 mm in length), with the core properties summarized in Table 1. To ensure that the permeability of the artificial fractures matched that of the target reservoir, quartz sand of different mesh sizes was used to fill the fractures. This method effectively simulated the fracture width of the actual reservoir while avoiding the interference of conventional iron spacers with the NMR measurements.

3.1.2. *Experimental fluids*

To eliminate the influence of hydrogen atoms in formation water on the NMR signal and ensure that the hydrogen signals originate exclusively from the oil phase, a deuterium water solution (D_2O) was used as the solvent to prepare the simulated formation water. The composition of the formation water ions in the target reservoir is listed in Table 2. The crude oil used in this experiment was a blend of condensate oil from the Dagang Oilfield (China) and No. 5 white oil, with a shear viscosity of 2 mPa·s and an oil–water interfacial tension of 0.076 N/m. Specifically, to enhance the grayscale contrast between oil and formation water in the CT images, 30 wt% potassium iodide (KI) was added to the simulated formation water. The strong X-ray absorption capacity of KI facilitated phase segmentation in the CT images.

3.2. *Experimental setup and procedures*

Fig. 2 illustrates the in-situ NMR/CT core displacement system, which consists of three main components: a fluid injection system, an in-situ NMR/CT measurement system, and a pressure sensing system. The fluid injection system includes an ISCO pump (Teledyne ISCO, USA) and a high-pressure intermediate container. By controlling different intermediate containers, the system facilitates the complete process from core saturation to displacement. The in-situ NMR measurement system features a key instrument, the MacroMR12-150H-I NMR spectrometer (Niumag, China). This device operates at a permanent magnetic field strength of 0.3 T with a resonance frequency of 12.79 MHz and supports experimental temperatures up to 80 °C. The core holder's confining pressure device uses hydrogen-free fluorinated fluids for both the confining pressure medium and magnetic constant-temperature

Table 1
Basic parameters of the experimental cores.

Core number	Depth, m	Geologic position	Lithology	Porosity ϕ, %	Permeability k, mD	Core picture
1	3028.2	A	Dolomites	10.53	2.59	
1f				10.76	108.20	
2	3124.0			14.26	0.49	
2f				14.52	101.43	
3	3136.0	B	Limestone	14.17	4.15	
3f				14.38	102.82	
4	3109.0			21.85	13.71	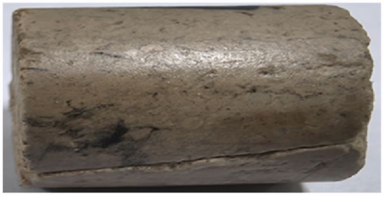
4f				22.09	119.73	

Table 2
Formation water composition.

Cation, mg/L				Anion, mg/L			Total mineralization, mg/L
Na^+	K^+	Ca^{2+}	Mg^{2+}	Cl^-	SO_4^{2-}	CO_3^{2-}	
66711.58	1177.09	13592.27	1752.39	145134.86	1109.25	422.54	229,899.98

fluid. The confining pressure device can withstand a maximum pressure of 40 MPa. The in-situ CT scanning system is equipped with a micron-scale CT scanner, specifically the nanoVoxel-3502E series (Sanying, China). During LTWF CT scans, the equipment operates at a voltage of 150 kV and a power of 10 W, with an exposure time of 0.5 s. The scanning resolution for all samples is set to 2 μm. The pressure sensing system comprises electronic pressure gauges and receivers, which enable real-time monitoring of pressure variations at various points. Additional equipment includes graduated cylinders, six-way valves, and a backpressure regulator. For HPMI, the AutoPore V 9600 instrument (Micromeritics, USA) was used. This instrument has a maximum pressure capacity of 420 MPa, allowing the measurement of pore-throat radii as small as 0.003 μm.

This study employs in-situ NMR and CT scanning technology to investigate the microscopic pore-throat displacement characteristics and residual oil dynamic evolution in a complex lithology reservoir in the Middle East under LTWF. The experimental procedure is as follows:

(1) To suppress water-phase signals and ensure that NMR signals originate solely from oil within the core, D_2O was used instead of distilled water as the solvent. Simulated formation water was prepared with matching salinity based on the ionic composition listed in the target block's formation water composition (Table 2). The simulated oil phase was a blend of Dagang condensate oil and No. 5 white oil, with a viscosity of 2 mPa·s.
(2) After cleaning, the cores were placed in a vacuum chamber and evacuated at −0.1 MPa for 5 h. Formation water was then backflushed into the vacuum chamber, and the cores were saturated for 24 h before removal.
(3) The saturated cores were encapsulated in thermoplastic material and placed in the NMR apparatus. A backpressure of 35 MPa was applied to simulate reservoir pressure conditions, with the confining pressure maintained 2 MPa higher than the injection pressure. Fluorinated fluids free of hydrogen signals were used to provide the confining pressure.
(4) Five pore volumes (PV) of simulated formation water were injected at a flow rate of 0.05 mL/min using an ISCO pump. Subsequently, the cores were saturated with oil at the same flow rate until no water was produced at the outlet. After establishing irreducible water saturation, the oil phase was aged for 14 d before performing the initial NMR scan.
(5) Simulated formation water was injected at a flow rate of 0.3 mL/min using the ISCO pump, with NMR scans conducted at displacement volumes of 1, 10, 30, 1000, and 2000 PV.
(6) Steps 1 through 5 were repeated for additional cores.

After completing the in-situ NMR displacement experiment, the core samples were subjected to an oil washing procedure using a 1:3 mixture of ethanol and toluene, following the standard GB/T 29172-2012. The cleaned cores were then recut, with one portion prepared according to the required dimensions for in-situ CT scanning (diameter: 5 mm, length: 10 mm), and another portion processed into standard samples for HPMI experiments (cores 1 and 4). The HPMI tests were conducted following the Chinese petroleum and natural gas industry standard GB/T 29171-2023. Notably, the subsequent in-situ CT scanning experiment followed a procedure similar to the in-situ NMR displacement experiment, with modifications in pressure and displacement rate. The displacement pressure was set to 12 MPa, and the two displacement rates were set at 0.03 and 0.3 mL/min. In-situ CT scanning was performed at key points: water flooding at 0 (saturated oil), 0.5, 10, and 1000 PV.

3.3. NMR principles and NMR T_2 conversion

Currently, HPMI experiments are widely employed to evaluate the pore structure of reservoir rocks. However, due to the inherent limitations of HPMI, mercury cannot fully penetrate all pore spaces within the rock under a given intrusion pressure, resulting in less

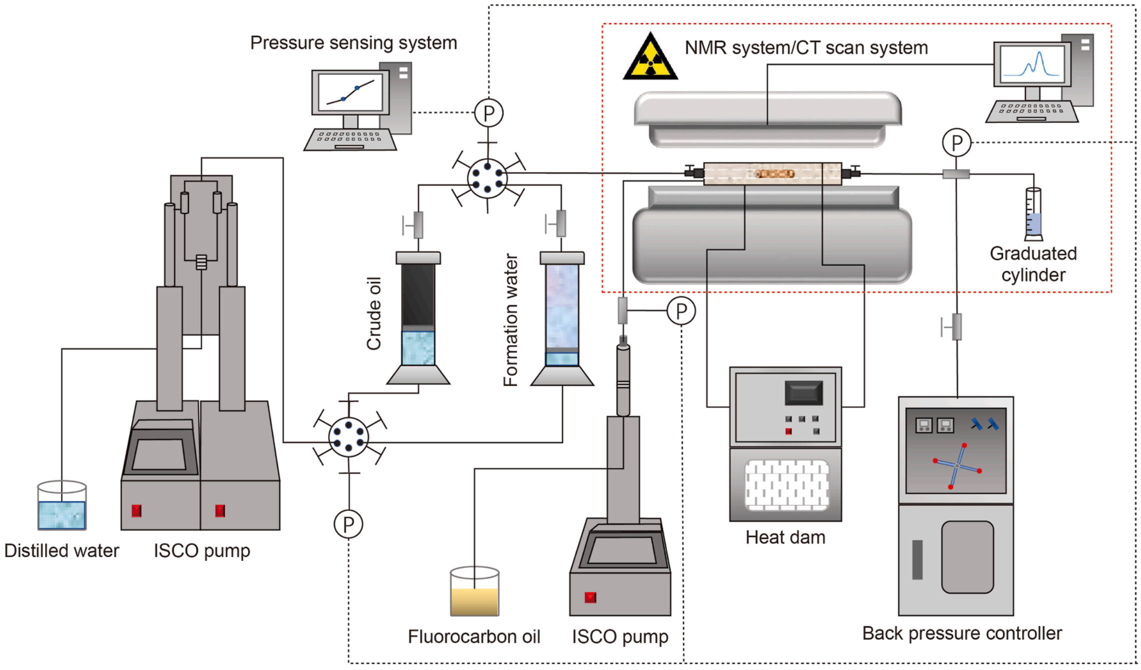

Fig. 2. Schematic of the in-situ NMR/CT scan core flooding imaging device.

than 100% mercury saturation. Specifically, mercury does not enter pores smaller than the pore-throat radius corresponding to the maximum applied intrusion pressure. Consequently, HPMI fails to provide a complete representation of the pore-throat distribution in the reservoir rock. According to NMR theory, the T_2 spectra obtained from rocks fully saturated with formation water can reveal information about the entire pore system. However, this approach cannot quantitatively characterize the pore structure. By integrating HPMI with NMR, the pore structure of carbonate reservoir rocks can be quantified effectively (Gao and Li, 2015; Zhang et al., 2024). Based on NMR theory and extensive studies, the T_2 of a single fluid in a porous medium under a uniform magnetic field can be expressed as follows:

$$\frac{1}{T_2}=\rho_2\frac{S}{V}=\rho_2\frac{F_s}{r_p} \tag{1}$$

where T_2 is the transverse relaxation time, ms; ρ_2 is the surface relaxivity, μm/ms; S is the surface area of the pore, cm^2; V is the pore volume, cm^3; F_s is the pore shape factor; and r_p is the pore radius, μm.

To achieve the transformation from NMR transverse relaxation time to pore size distribution, many researchers have constructed conversion relationships using HPMI pore size distributions that resemble the shape of NMR T_2 spectra. However, due to the complex pore structures in carbonate reservoirs, conventional linear conversion methods often fail to yield satisfactory results, leading to significant discrepancies with the actual HPMI pore size distributions (Benavides et al., 2017; Washburn et al., 2017). Through extensive analysis of NMR T_2 spectra and corresponding HPMI pore size distribution curves, we have proposed using nonlinear power functions for the conversion of T_2 spectra (Pan et al., 2024). The nonlinear transformation relationship can be expressed as

$$T_2=\frac{r_p^n}{\rho_2 F_s} \tag{2}$$

This method provides a more accurate correlation between NMR relaxation time and pore size distributions, reflecting the complex pore-throat characteristics of carbonate reservoir rocks. Using the relationship where the pore radius (r_p) is equal to the product of the pore-throat radius (r_t) and the pore-to-throat ratio (c), the equation can be transformed accordingly. Thus, Eq. (2) becomes

$$T_2=\frac{(cr_t)^n}{\rho_2 F_s} \tag{3}$$

where r_t is the pore-throat radius, μm; and c is the pore-to-throat ratio.

Let $C=(\rho_2 F_s)^{1/n}/c$, then Eq. (3) can be transformed into

$$r_t=CT_2^{1/n} \tag{4}$$

Taking the natural logarithm of both sides of Eq. (4), we obtain

$$\ln r_t=\ln C+\frac{1}{n}\ln T_2 \tag{5}$$

By jointly solving the NMR relaxation time distribution curve and the HPMI pore-throat distribution curve, the parameters C and n can be determined. Once these values are obtained, the transverse relaxation time distribution curve of the core fully saturated with formation water can be transformed into a pore-throat radius distribution curve.

3.4. CT data image processing

The original CT scan images primarily contain water, oil, and the rock matrix. However, due to the wide grayscale distribution of the rock matrix and the overlapping grayscale values at the oil–water interface, it is difficult to distinguish and effectively segment different phases and their interfaces. Therefore, specialized image processing software is required to process the raw CT images. In this study, Avizo software was used for image processing and analysis. Uncontrollable factors such as experimental conditions, rock physical properties, and CT equipment can introduce noise and ring artifacts into the images, affecting the accuracy and precision of subsequent image segmentation. Filtering is an effective method to address these issues. In this study, the non-local means filtering method was used. This method, based on image similarity, smooths the image by identifying similar patches throughout the image while preserving texture and details, making it one of the most commonly used filtering techniques. Fig. 3(a) and (b) show the original and filtered images, respectively. After noise reduction, the images were segmented into oil and water phases using the watershed segmentation method. The watershed algorithm is a classic image segmentation technique that simulates the process of water flowing over a terrain to form watersheds, thereby dividing the image into distinct regions or objects. To ensure segmentation accuracy, the volume of oil obtained from the segmented digital core was compared with the actual oil volume displaced from the core. In this study, seed points (oil and water phases) were manually selected, and then image recognition was performed using the semi-automatic watershed algorithm.

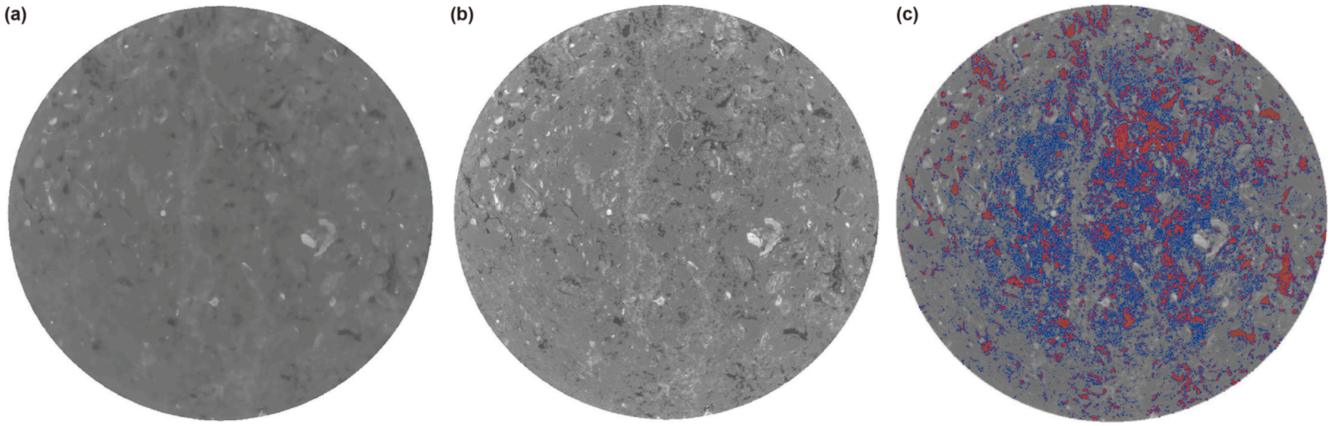

Fig. 3. Image processing workflow. (**a**) Original image; (**b**) filter smoothing; (**c**) segmented image (red: oil; blue: water).

The semi-automatic watershed algorithm was iteratively adjusted based on the discrepancy between the calculated and actual values to achieve an optimal segmentation state. Additionally, the dice coefficient was introduced to effectively evaluate the image recognition accuracy. In this study, the final oil-phase recognition rate (dice coefficient) reached 0.89, demonstrating the accuracy and reliability of the CT image segmentation methodology. Fig. 3(c) shows the segmented image using the watershed algorithm, where red represents oil and blue represents water.

4. Results and discussion

4.1. HPMI analysis of pore-throat structure characteristics

HPMI is one of the commonly used methods in the oil and gas industry for analyzing pore structure. It is widely applied to describe the pore radius distribution characteristics of both conventional and unconventional reservoir rocks. As a non-wetting phase, mercury does not enter the pores of the rock spontaneously due to capillary forces; it can only be forced into the pores under applied external pressure. With increasing injection pressure, mercury overcomes the additional resistance at pore throats and enters smaller pores. Based on the assumption of cylindrical pores, Washburn established the relationship between mercury pressure and pore-throat radius (Wang et al., 2025):

$$P_c = \frac{2\sigma\cos\theta}{r_t} \tag{6}$$

where P_c is the capillary force, Pa; σ is the interfacial tension, mN/m; and θ is the contact angle.

Consequently, HPMI experiments provide valuable data on pore-throat radius distribution and related pore structure parameters for reservoir rocks. Fig. 4 presents the mercury capillary pressure curves for all core samples and the pore-throat radius distribution curves derived using Eq. (6). Table 3 summarizes the pore structure parameters of the core samples.

The capillary pressure curves obtained from the HPMI experiments are shown in Fig. 4(a). The curves reveal that the mercury saturation increases with rising capillary pressure. For cores of the same lithology, as the permeability decreases, the petrophysical properties deteriorate, causing the capillary pressure curves to shift upward overall. When the reservoir rock exhibits poor sorting, the capillary pressure curves for limestone cores 1 and 2 display a dual-step trend. This suggests that the limestone reservoir contains both large and small pore throats, indicating a certain degree of microscopic heterogeneity in the limestone formations.

The pore structure parameters derived from the HPMI experiments include displacement pressure, maximum mercury saturation, and median pressure, which characterize the complexity of reservoir pore structures. Maximum pore radius, average pore radius, and median pore radius describe the size of pores in the cores, while sorting coefficient, homogeneity coefficient, and skewness characterize the distribution of pore sizes. In this study, displacement pressure, average pore-throat diameter, and sorting coefficient were selected for comprehensive analysis of pore structures in different reservoir rock types. A lower displacement pressure indicates better core connectivity, a larger average pore-throat diameter suggests a larger overall pore size, and a smaller sorting coefficient reflects more uniform pore distribution with pore sizes concentrated in a narrower range. Using the pore structure parameters in Table 3, the differences in pore structure characteristics among various reservoir rock types can be quantitatively analyzed. Dolomite cores (cores 1 and 2) exhibit an average displacement pressure of 1.01 MPa, while limestone cores (cores 3 and 4) have an average displacement pressure of 0.22 MPa. The higher displacement pressure of dolomite indicates poorer connectivity compared to limestone. The average pore-throat radius for dolomite is 0.25 μm, whereas it is 0.43 μm for limestone, suggesting that the overall permeability of limestone

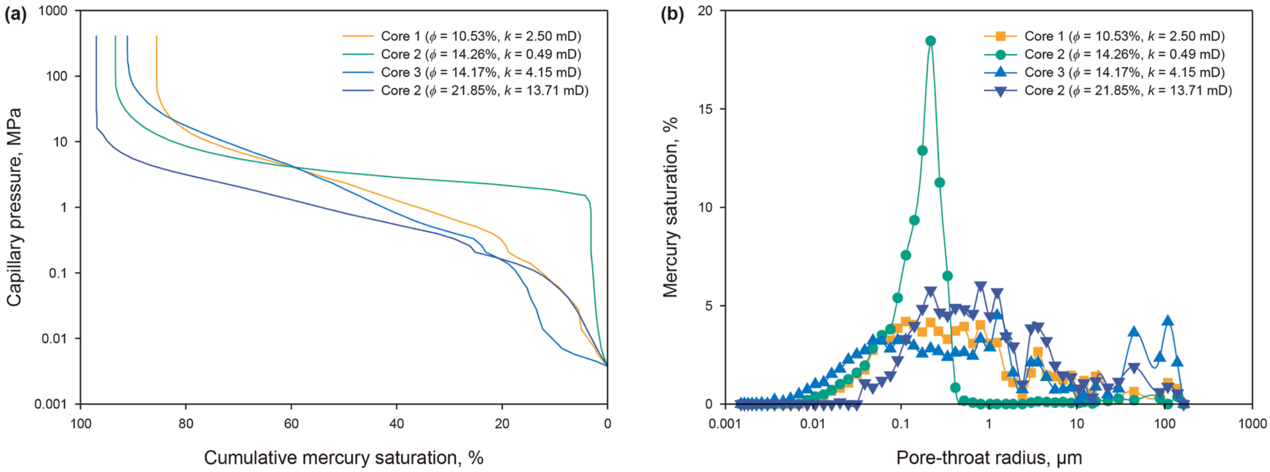

Fig. 4. HPMI experiment data. (**a**) HPMI capillary pressure curve; (**b**) pore-throat radius distribution curve.

Table 3
Core HPMI characteristic parameters.

Core number	Displacement pressure, MPa	Median pressure, MPa	Maximum pore-throat radius, μm	Average pore-throat radius, μm	Skewness	Sorting coefficient
1	0.523	3.394	1.325	0.265	0.215	2.214
2	1.500	5.015	0.415	0.226	0.132	1.251
3	0.276	1.920	2.368	0.362	0.324	3.124
4	0.165	1.732	4.134	0.504	0.687	1.632

reservoirs is higher than that of dolomite reservoirs. The average sorting coefficient for dolomite is 1.73, while for limestone, it is 2.38. The lower sorting coefficient of dolomite indicates the presence of dominant pore throats of a particular size and a more uniform pore size distribution. Using the Washburn equation (Eq. (6)), the capillary pressure curves were converted to pore-throat radius distribution curves, as shown in Fig. 4(b). The pore-throat radii for dolomite cores (cores 1 and 2) predominantly range from 0.1 to 10 μm, displaying a unimodal distribution. In contrast, limestone cores (cores 3 and 4) exhibit a bimodal distribution, with the first peak in the range of 0.1–5 μm and the second peak between 50 and 200 μm. This bimodal behavior in limestone indicates a wider range of dominant pore-throat radii. The second peak in limestone, corresponding to larger pore throats with lower flow resistance, highlights the superior permeability of limestone reservoirs compared to dolomite reservoirs.

4.2. NMR analysis of microscopic pore-throat displacement characteristics

4.2.1. NMR T_2 conversion

Due to the complexity of the pore structure in carbonate reservoirs, the mercury intrusion capillary pressure method can only reflect pore throat information corresponding to radii smaller than the maximum mercury intrusion pressure, while the core's NMR T_2 spectrum, when 100% saturated with formation water, can theoretically reflect the information for all pore throats. Therefore, the pore throat range obtained by mercury intrusion is narrower than that obtained by NMR. To minimize errors in both physical meaning and geometric shape between the two curves, the comparison is made using the mercury intrusion pore-throat radius distribution corresponding to a saturation below the maximum mercury saturation, which is then compared with the NMR T_2 spectrum. The specific process is as follows:

(1) Plot the cumulative distribution curves of the mercury intrusion pore-throat radius and NMR T_2 relaxation time, as shown in Fig. 5(a).
(2) In the region corresponding to mercury saturation lower than the maximum mercury saturation, select any pore-throat radius $r_t(i)$ with cumulative frequency $S(i)$, and interpolate the T_2 spectrum using $S(i)$ to obtain the T_2 value $T_2(i)$ corresponding to the selected $r_t(i)$.
(3) Using the least squares method, fit the parameters of Eq. (5) to obtain the C and n values that minimize the error.

The cumulative distribution curve of the NMR relaxation time and the cumulative distribution curve of the mercury intrusion pore-throat radii for core 1 were selected to calibrate the relationship between relaxation time and pore-throat radius. From the fitting results (Fig. 5(b)), it is evident that the test data and the fitted line show a good morphological consistency, with a curve fitting degree of 98.9%, indicating a high fitting accuracy and proving the rationality of the fitting method. By substituting $C = 0.0071$ and $n = 1.0836$ into Eq. (4), the horizontal axis of the T_2 spectrum can be transformed from relaxation time to pore-throat radius distribution.

4.2.2. NMR core flooding characteristics

In the field of petroleum engineering, the NMR T_2 spectrum can quantitatively characterize the pore-throat distribution, fluid distribution, and fluid displacement characteristics of a core sample. In this experiment, by calculating the ratio of the area under the NMR T_2 spectrum at different waterflooding volumes to the area under the NMR T_2 spectrum at the saturated oil state, the stage oil recovery efficiency of the core sample under different waterflooding volumes can be determined.

4.2.2.1. Effect of lithology on oil recovery efficiency. The members A and B of the Asmari Formation in the A oilfield of Iraq are the primary production zones of the field and the target layers of this study. The member A is mainly composed of dolomite, while the member B is predominantly limestone. To investigate the impact of long-term waterflooding on oil recovery efficiency in two different lithologies, this study conducted in-situ NMR displacement experiments using two core samples with different permeability from both the members A and B of the A oilfield. Fig. 6 and Table 4 show the NMR T_2 spectra and oil recovery efficiency changes of the experimental cores at different displacement stages. As the displacement volume increases, both dolomite and limestone cores show varying degrees of increased displacement efficiency, with the limestone cores exhibiting a significantly higher oil recovery efficiency compared to the dolomite cores. Analysis of high-pressure mercury intrusion experiments indicates that the limestone reservoir has better-developed pores, larger pore space, larger pore-throat radius, and stronger permeability, suggesting that the reservoir quality is superior to that of the dolomite reservoir. This is consistent with the higher oil recovery efficiency observed for the limestone reservoir in the displacement experiments. Within the same lithology, cores with better permeability exhibit higher oil recovery efficiency, which aligns with existing

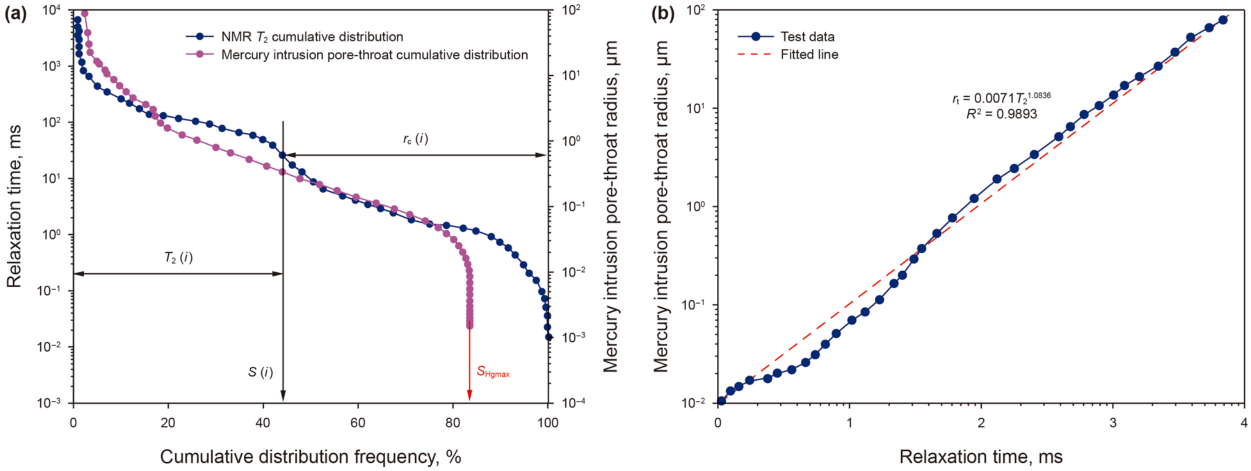

Fig. 5. Transforming NMR T_2 to throat radius. (**a**) Cumulative distribution curves of relaxation time and pore-throat radius; (**b**) fitting of conversion coefficients.

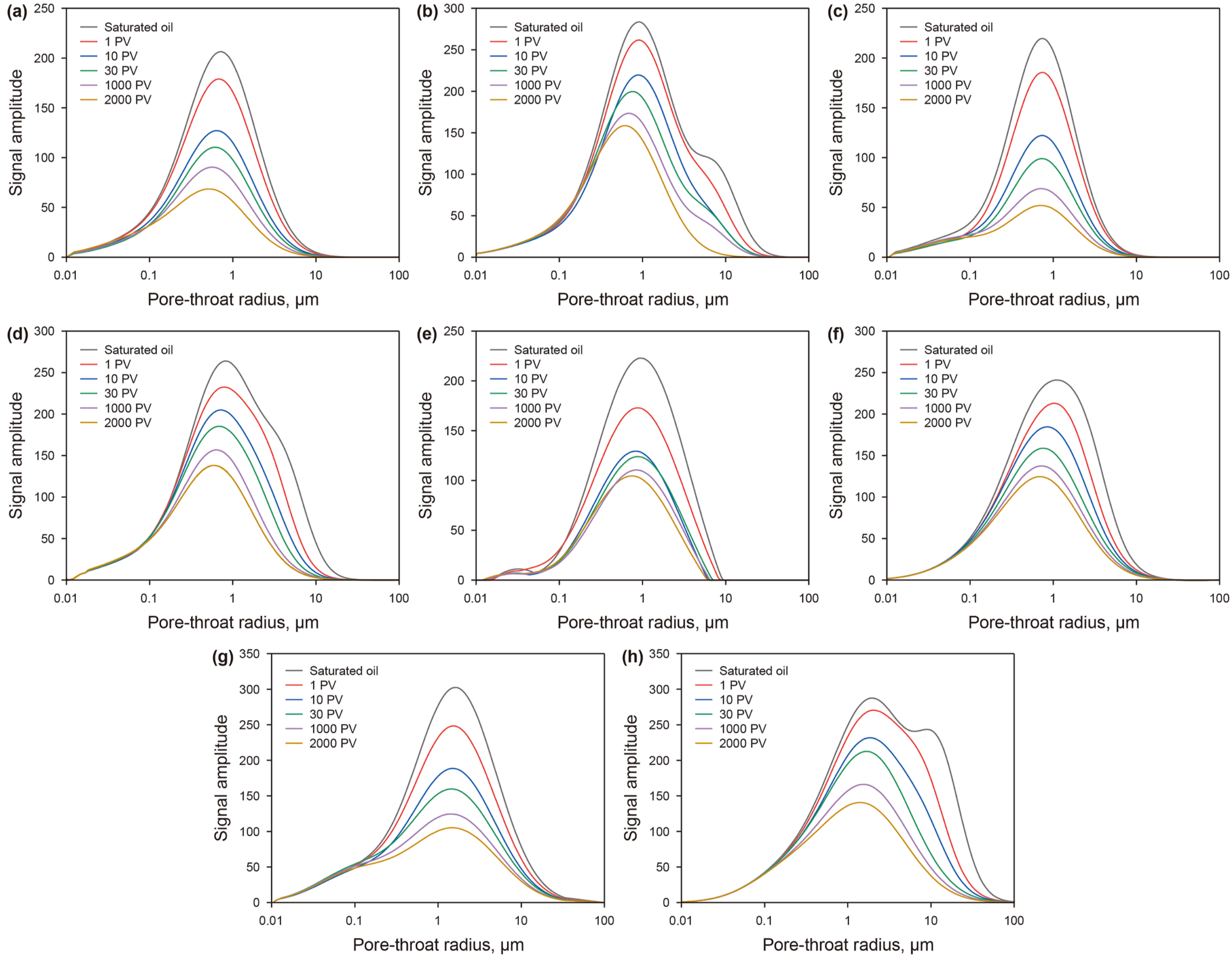

Fig. 6. NMR T_2 spectra of different experimental core samples. (**a**) Core 1; (**b**) Core 1f; (**c**) Core 2; (**d**) Core 2f; (**e**) Core 3; (**f**) Core 3f; (**g**) Core 4; (**h**) Core 4f.

Table 4
Core oil recovery efficiency at different displacement stages.

Displacement stage	Oil recovery efficiency, %							
	Core 1	Core 1f	Core 2	Core 2f	Core 3	Core 3f	Core 4	Core 4f
1 PV	17.2	12.5	15.6	11.2	18.7	13.6	19.6	16.8
10 PV	45.7	38.5	42.5	37.3	46.8	38.6	52.4	44.3
30 PV	48.6	41.7	46.8	40.2	50.6	43.6	57.6	49.7
1000 PV	51.1	46.2	48.5	50.3	51.3	48.5	60.3	55.4
2000 PV	54.3	49.6	51.2	52.1	52.6	50.8	62.6	58.3

knowledge. When the displacement volume reaches 2000 PV, the maximum oil recovery for the limestone core (core 4) is 62.6%, while for the dolomite core (core 1), the maximum recovery is 54.3%. The oil recovery of the limestone core is about 8% higher than that of the dolomite core. Importantly, in the actual waterflooding development of carbonate reservoirs, the limestone reservoir of member B, due to its better reservoir quality, becomes waterflooded earlier, leading to a lower degree of oil utilization in the dolomite reservoir of member A. Therefore, timely water shutoff and profile modification should be implemented to improve the macro sweep efficiency of the A oilfield reservoir, ultimately increasing the oil recovery rate in the field.

By comparing the oil recovery efficiency of different lithology matrix cores at various waterflooding volumes, it is observed that as the waterflooding volume increases, the oil recovery also increases. However, when the waterflooding volume exceeds 30 PV, the increase in oil recovery efficiency slows down. At the waterflooding volume of 30 PV, the highest oil recovery efficiency for dolomite is 48.6%, while for limestone it is 57.6%. However, when the waterflooding volume increases to 1000 PV, the oil recovery efficiency for dolomite can only increase by 5%, and for limestone, it only increases by 4%. If the displacement volume is further increased to 2000 PV, the maximum oil recovery efficiency improvement is 3%. The experimental results show that the oil recovery efficiency of long-term waterflooding in carbonate reservoirs is lower than that in conventional sandstone reservoirs. Analysis suggests that the wettability of conventional sandstone reservoirs is primarily water-wet, where oil in the pores undergoes capillary suction with formation water, effectively displacing the oil. As a result, waterflooding leads to high oil recovery efficiency. However, in carbonate reservoirs, the wettability is typically mixed-wet or oil-wet, making it more difficult to displace the oil from the pores. Additionally, the highly developed fracture systems in carbonate reservoirs prevent formation water from effectively displacing the oil in the reservoir matrix.

4.2.2.2. Effect of fractures on oil recovery efficiency. Compared to conventional sandstone reservoirs, carbonate reservoirs have complex pore structures, and the highly developed fractures allow formation water to flow along the fractures, resulting in the inability to effectively utilize oil in certain areas of the reservoir. The lithology and pore structure of the A oilfield in Iraq are complex, with a high degree of fracture development. The dynamic performance of the reservoir shows a rapid water cut increase and a sharp decline, characteristic of many carbonate reservoirs. To investigate the impact of fractures in LTWF in carbonate reservoirs, this study created fractured core samples with an equivalent fracture permeability based on the fracture information of the A oilfield, and using a similar permeability constraint with the original matrix cores by cutting and filling them with different mesh sizes of quartz sand.

The experimental results indicate that the oil recovery efficiency of the fractured core is significantly lower than that of the matrix core. When the displacement volume is 2000 PV, the oil recovery efficiency decreases by approximately 5%. The analysis suggests that fractures, as the main flow path for fluids in the core, not only increase the core permeability but also limit the ability of the displacement fluid to utilize the oil in the matrix, leading to lower oil recovery efficiency. Additionally, due to the mixed-wet or oil-wet nature of carbonate reservoirs, the capillary suction phenomenon typical of conventional sandstone reservoirs does not occur, making it more difficult to displace the oil in the pores. Thus, in carbonate reservoirs undergoing long-term water flooding, the implementation of complementary technologies, such as surfactant injection or CO_2 flooding, is recommended to improve sweep efficiency and ultimate oil recovery.

4.2.3. Microscopic pore-throat utilization characteristics

The microscopic pore-throat utilization characteristics of core samples are important parameters and indicators to assess the LTWF effectiveness in carbonate reservoirs. They also provide a theoretical basis for understanding the distribution and potential recovery of residual oil after LTWF. To classify the pores in the reservoir, Hu et al. (2020) applied five models to fit the fractal characteristics of the reservoir, using the pore-throat radius as a boundary to categorize the pores into nanopores (< 0.1 μm), submicron pores (0.1–1 μm), microscale micropores (1–10 μm), and microscale macropores (> 10 μm). To determine the degree of oil recovery in different scale pore throats at various displacement stages, the NMR T_2 spectra shown in Fig. 6 were used. The areas corresponding to different scale pore throats at various displacement stages were calculated and compared to the area at the saturated oil state. This provides the degree of oil recovery in different pore throat scales under various displacement conditions. Table 5 summarizes the microscopic pore-throat utilization characteristics of the core samples for different displacement stages.

From the LTWF NMR T_2 spectra of different core samples, it can be observed that the overall pore structure of the core changes after fracturing. This is reflected in the increased signal intensity at the micron micropore region in the NMR T_2 spectra, indicating a change in the oil distribution state in the core. The amount of oil in the large pores increases. Additionally, with the increase in water injection volume, the oil recovery in microscale micropores and microscale macropores is higher, while oil in nanopores is almost entirely unrecovered. When the displacement volume reaches 1000 PV, the oil recovery in microscale micropores and microscale macropores decreases, but the oil recovery in submicron pores improves. Careful observation of the NMR T_2 spectra reveals a trend of the peak shifting leftward with the increase in water injection volume. It is believed that, after the injection of formation water into the core, the oil is primarily displaced by the leading edge of the injected front. Due to the pressure gradient, the formation water preferentially displaces oil from the microscale micropores and microscale macropores, which have lower additional resistance. As a result, the NMR signal from these pores decreases significantly. Simultaneously, as the displacement progresses, the formation water drives the oil to migrate into smaller-scale pores, leading to a slight leftward shift of the peak in the NMR T_2 spectra.

To visually describe the contribution of different pore levels to oil recovery efficiency in various experiments, the data from Table 5 was processed and visualized, resulting in the oil recovery degree map for each pore throat level shown in Fig. 7. Since waterflooding cannot effectively utilize oil from nanopores, only the contributions of submicron pores, microscale micropores, and microscale macropores to the oil recovery of the core were considered in the plot. By combining the data from Table 5 and Fig. 7, it can be observed that for the matrix core, high water injection volume (2000 PV) mainly utilizes oil from submicron pores and microscale micropores, with the maximum recovery from submicron pores and microscale micropores being 27.5% and 36.8%, respectively. For the fractured core, due to significant changes in pore structure, the proportion of microscale macropores increases. High water injection volume (2000 PV) mainly utilizes oil from microscale micropores and microscale macropores, with the maximum recovery from microscale micropores and microscale macropores being 30.2% and 17.6%, respectively. Additionally, by analyzing the trend of oil recovery from different pore levels in both matrix and fractured cores during LTWF, it is

Table 5
Microscopic pore-throat utilization characteristics of the core samples.

Core number	Oil recovery from different pores, %											
	Nanopores			Submicron pores			Microscale micropores			Microscale macropores		
	30 PV	1000 PV	2000 PV	30 PV	1000 PV	2000 PV	30 PV	1000 PV	2000 PV	30 PV	1000 PV	2000 PV
1	1.3	1.4	1.5	19.6	20.5	22.1	27.6	29.1	30.6	0.1	0.1	0.1
1f	0.2	0.3	0.4	12.7	13.5	14.1	24.8	25.2	27.9	8.9	9.1	9.8
2	1.2	1.3	1.4	19.8	20.6	21.7	25.7	26.5	27.8	0.1	0.1	0.1
2f	0.2	0.3	0.3	13.3	17.2	18.0	23.4	29.3	30.2	3.3	3.5	3.6
3	0.6	0.6	0.6	26.6	27.0	27.5	23.3	23.6	24.4	0.1	0.1	0.1
3f	0.1	0.1	0.1	17.8	20.2	22.0	25.3	27.8	28.3	0.4	0.4	0.4
4	0.1	0.1	0.1	20.3	21.2	22.1	34.0	35.5	36.8	3.2	3.5	3.6
4f	0.1	0.1	0.1	10.8	12.6	13.4	22.5	25.6	27.2	16.3	17.1	17.6

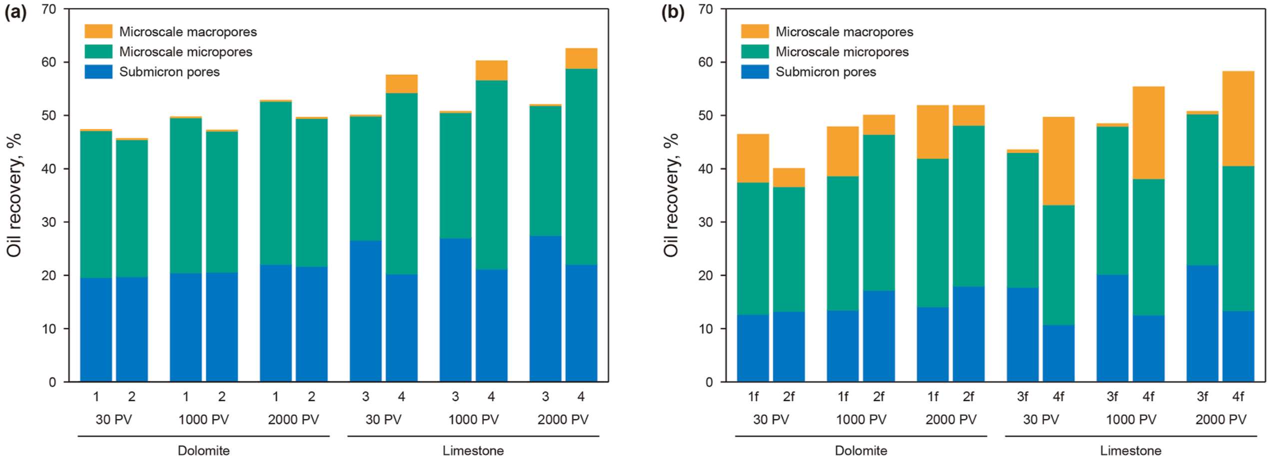

Fig. 7. The oil recovery efficiency by different pore size hierarchies. (**a**) Matrix core; (**b**) fracture core.

evident that microscale micropores and microscale macropores are the main contributors to the recovery factor. As the displacement volume increases, the recovery of oil from submicron pores gradually increases, though oil in nanopores remains largely unrecovered. Therefore, improving the producing of oil from nanopores and submicron pores in carbonate reservoirs is key to enhancing recovery rates. In the later stages of development, displacement technologies such as surfactant flooding or CO_2 flooding could be considered to enhance oil producing from nanopores and submicron pores.

Compared with relatively homogeneous sandstone reservoirs with well-developed pore-throat structures, carbonate reservoirs exhibit markedly different microscopic pore-throat displacement characteristics during LTWF. In sandstones, waterflooding typically proceeds in a relatively uniform piston-like manner, leading to a balanced utilization of pores across scales and thus higher displacement efficiency. In contrast, the present study reveals that carbonates display pronounced heterogeneity and a hierarchical utilization pattern: injected water preferentially invades favorable channels and displaces oil from microscale macropores and microscale micropores, before slowly accessing a fraction of the submicron pores, while oil residing in nanopores remains almost entirely unrecovered. This phenomenon arises from the strong capillary pressure contrasts and wettability heterogeneity inherent in the complex pore architecture of carbonate rocks. Moreover, the presence of fractures further amplifies the uneven utilization by concentrating displacement around fracture-adjacent macropores. Therefore, residual oil in carbonate reservoirs is retained not only within nanopores but also extensively throughout a broader spectrum of unswept pore sizes. Such a complex utilization mechanism highlights that enhancing oil recovery in carbonate reservoirs requires targeted approaches—such as chemical flooding capable of effectively reducing interfacial tension and altering wettability—rather than a simple continuation of development strategies proven effective in sandstone reservoirs.

4.3. CT analysis of residual oil

4.3.1. Representative elementary volume

As the amount of data increases, CT scan images can reconstruct the state of the core at a given moment as accurately as possible. However, due to computational limitations, it is not feasible to process the entire dataset at once. To address this constraint while ensuring the accurate calculation of core characteristic parameters, it is necessary to appropriately compress and filter the original dataset, selecting representative volume elements (REV) for image processing. A REV is a subunit extracted from any location within the original dataset. The selected unit should be as small as possible while maintaining consistency with the overall core properties. This approach significantly improves computational efficiency and optimizes resource utilization. The same REV is extracted from the same location at different displacement stages, enabling the study of microscopic residual oil variations at specific positions and revealing its dynamic evolution under LTWF. In this study, a series of data cubes with different lengths were extracted using porosity as a parameter, and the porosity at different scales was calculated for each cube. Although a larger dataset allows a more comprehensive representation of core characteristics, computational capacity may not support processing the entire experimental core dataset simultaneously. Therefore, to align with computational constraints, representative volume elements were selected as the smallest units that effectively characterize the physical properties of the core. The objective is to ensure that the physical properties derived from the smallest representative unit remain consistent with those of the entire core. By using porosity as parameter, a series of three-dimensional data cubes of varying sizes were extracted, and their porosity values were calculated. The results

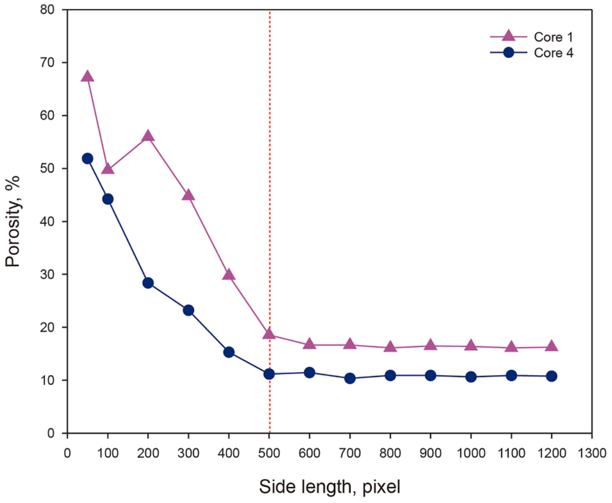

Fig. 8. Representative elementary volume.

indicate that as the dataset size increases, the curves gradually stabilize. The critical point at which the curve levels off is taken as the representative volume element, ensuring that this unit accurately reflects the true characteristics of the entire core.

The size of the REV is crucial for ensuring the reliability of experimental analysis results. Previous studies have indicated that when the REV size exceeds 400 μm, it can effectively represent porosity, while a REV size greater than 800 μm is required to accurately characterize permeability (Mostaghimi et al., 2013). As shown in Fig. 8, the experimental results of this study demonstrate that as the grid size increases, the parameter curves gradually stabilize when the scanned cubic volume exceeds 500 pixels in length. Based on this observation, the fundamental research unit for this study is determined to be a cube with a side length of 500 pixels (2 μm). In this study, the selected REV grid size is 500 pixels × 500 pixels × 500 pixels, corresponding to an actual physical dimension of 1000 μm × 1000 μm × 1000 μm. This selection enhances the accuracy of phase segmentation and improves the reliability of the experimental results.

4.3.2. *Microscopic residual oil classification*

During the water flooding process, residual oil is distributed in different forms across various locations within the porous medium, primarily in large pores, throats, and along pore walls. In this study, to better characterize different types of residual oil, we adopted the classification method proposed by Liu et al. (2023) and defined five distinct types of residual oil based on three parameters: shape factor, Euler number, and contact ratio. The shape factor reflects the resemblance of an individual residual oil droplet to a sphere. A shape factor of 1 indicates a perfectly spherical residual oil droplet. The shape factor is defined as (Li et al., 2012)

$$G_f = \frac{6\sqrt{\pi}V}{S^{1.5}} \tag{7}$$

where G_f is the shape factor; V is the volume of oil, μm^3; S is the surface area of oil, μm^2.

The Euler number is commonly used to characterize the connectivity of residual oil. A lower Euler number indicates better connectivity of the residual oil. The Euler number can be defined as (Qin et al., 2022)

$$E = 1 - b_1 + b_2 \tag{8}$$

where E is the Euler number of the oil cluster; b_1 is the number of connectivity; b_2 is the enclosed cavities.

The contact ratio reflects the interaction between an individual residual oil cluster and the pore wall (Li et al., 2017). A smaller contact ratio indicates a lower proportion of residual oil adhering to the pore surface. The contact ratio can be defined as

$$C_r = \frac{S_c}{S} \tag{9}$$

where C_r is the contact ratio of the oil cluster; S_c is the surface area between an individual residual oil cluster and the pore wall, μm^2.

Based on the shape factor, Euler number, and contact ratio, combined with the formation mechanisms of residual oil, residual oil can be classified into three main types with five specific forms: clustered, throat, droplet, corner adsorbed, and pore lining. Among them, clustered and throat residual oil belong to the bypassed type, droplet residual oil is classified as the blockage type, and corner adsorbed and pore lining residual oil fall under the adsorption type. The detailed classification is illustrated in Table 6, and the shape factor, Euler number, and contact ratio were calculated using the label analysis module in Avizo software.

4.3.3. *Dynamic evolution characteristics of microscopic residual oil*

The Avizo software was used to process images of the REV under different water injection volumes. By utilizing the label analysis module in combination with the five types of microscopic residual oil classification proposed in this study, the distribution of different types of residual oil at various injection volume values was visually presented, as shown in Figs. 9 and 10. Additionally, the relative proportions of the five types of residual oil at different displacement stages were quantitatively analyzed, with the results summarized in Table 7. The study revealed that for both dolomite and limestone cores, the overall oil saturation decreased with increasing volume of injected water, accompanied by significant morphological changes in the residual oil. Specifically, as water injection progressed, continuous-phase residual oil (clustered form) increasingly transformed into the four other types of discontinuous-phase residual oil. This phenomenon is attributed to the heterogeneity of carbonate rocks, which leads to localized increases in density and decreases in pore-throat size. Given that carbonate reservoirs in the Middle East are predominantly oil-wet, injected water tends to preferentially flow through large pore channels with lower capillary resistance (high permeability channel), leaving oil trapped in smaller pores that remain unswept, ultimately forming residual oil. For discontinuous-phase residual oil, the oil-wet nature of the rock causes crude oil to adhere to pore and throat surfaces. When the adhesion force between crude oil and the rock surface exceeds the displacement force exerted by water injection, the oil remains attached to the rock, forming oil films. This trend is also evident in Table 7, which shows that adsorbed residual oil (corner adsorbed and pore lining types) accounts for the largest proportion at high water injection volumes, exceeding 25%.

By comparing the microscopic residual oil distribution in dolomite and limestone under different injection volumes of water (Table 7), the differences in residual oil evolution under high water injection volumes in the Middle East can be clearly identified. The distribution characteristics of residual oil in dolomite and limestone exhibit significant differences at various displacement stages, with their evolution jointly controlled by pore structure and wettability. At low displacement volume (0.5 PV), the reduction in clustered residual oil in limestone (5.3%) is slightly higher

Table 6
Classification standard of microscopic residual oil.

Formation mechanism	Residual oil type	Standard of classification		
		Shape factor	Euler number	Contact ratio
Bypassed type	Clustered	$G > 2$	$E \leq -1$	$C > 0.4$
	Throat	$G > 2$	$E > 0$	$C > 0.4$
Blockage type	Droplet	$G \leq 2$	$E > 0$	$C < 0.1$
Adsorption type	Corner adsorbed	$G > 2$	$E > 0$	$0.5 > C > 0.4$
	Pore lining	$G > 2$	$E > 0$	$C < 0.4$

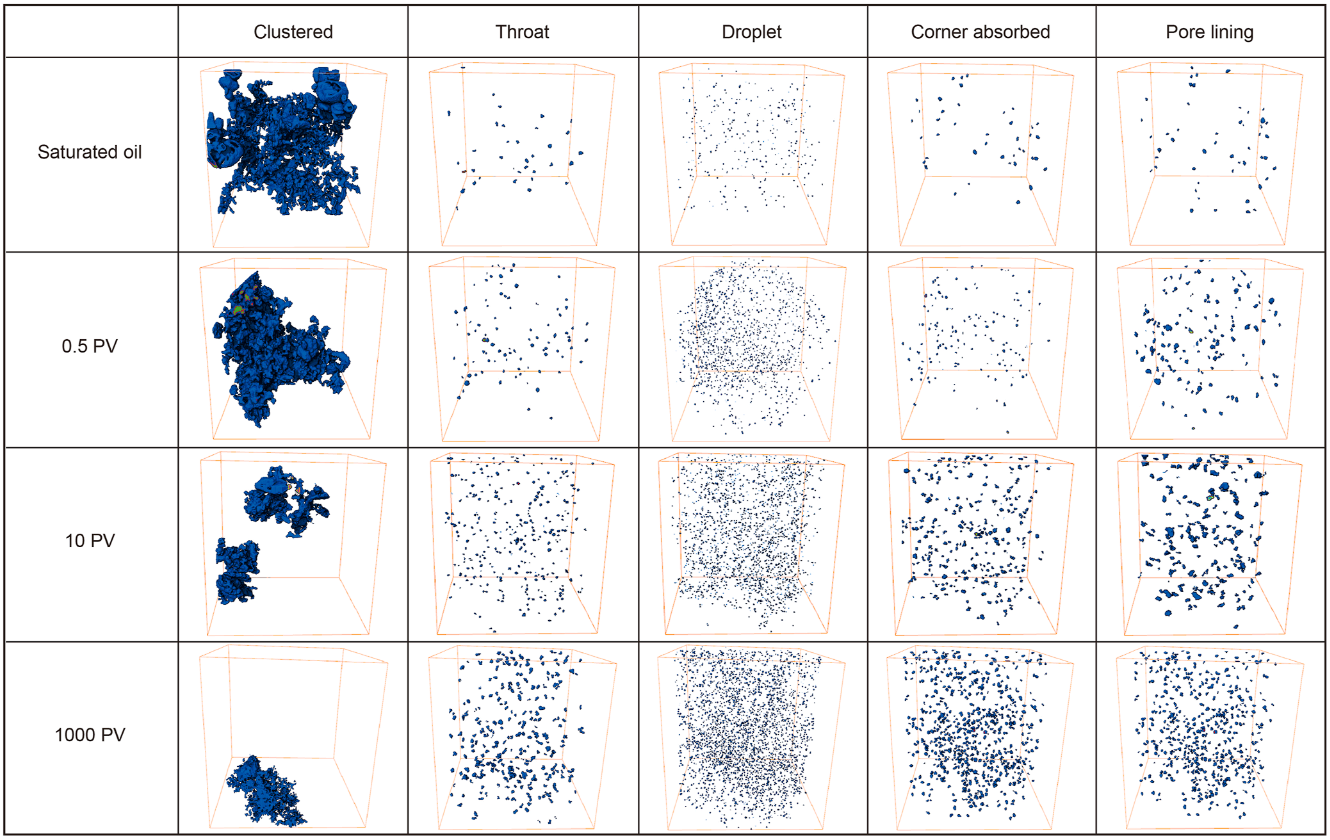

Fig. 9. Visualization of residual oil in dolomite core (core 1) during LTWF.

than that in dolomite (4.5%), while the proportion of throat residual oil continues to increase, highlighting the throat retention effect. In the mid-to-high displacement stages (10–1000 PV), the proportion of clustered residual oil in dolomite decreases from 68.6% to 55.3%, but it remains higher than that in limestone (52.8%), indicating the presence of large uncontacted pore regions in dolomite. In contrast, at 1000 PV, the proportion of corner adsorbed residual oil (12.2%) and pore lining residual oil (16.7%) in limestone is significantly higher than that in dolomite (10.7% and 15.2%, respectively), revealing that microscopic heterogeneity and surface wettability promote oil adhesion in pore corners and on mineral surfaces. In summary, for dolomite, as the water injection volume increases, the proportion of clustered residual oil decreases, while other types of residual oil increase. Due to its poorer petrophysical properties, the distribution of the four non-clustered residual oil types is relatively uniform. The transition of residual oil from clustered to throat forms suggests poor connectivity of residual oil, indicating that enhancing microscopic displacement efficiency should be the primary strategy for further residual oil recovery in dolomite reservoirs. For limestone, which has better petrophysical properties, the transformation of clustered residual oil into other non-clustered residual oil types is more pronounced. Since carbonate rocks in the Middle East are predominantly oil-wet, capillary forces act as a resistance to oil displacement. With increasing water injection volumes, the proportion of adsorbed residual oil (corner adsorbed + pore lining) becomes more dominant, exceeding 30%. Consequently, for this type of residual oil, enhancing oil displacement efficiency should be the key focus for further recovery.

In contrast to sandstone reservoirs, where residual oil after LTWF is predominantly distributed in isolated and clustered forms within pore throats with relatively uniform patterns, the microscopic evolution of residual oil in carbonate reservoirs revealed in this study exhibits significant differences. Strong heterogeneity and oil-wet characteristics drive a drastic transformation of residual oil morphology from continuous phases (clustered) to discontinuous phases (throat, corner adsorbed, and pore lining). Notably, adsorption-type residual oil (corner adsorbed + pore lining) accounts for more than 25% during LTWF, becoming the dominant form. This phenomenon stands in sharp contrast to sandstone reservoirs, where residual oil mainly exists as thin water films on grain surfaces and isolated oil droplets in pore throats. Specifically, dolomite, due to its poorer physical properties, demonstrates a disruption of clustered residual oil continuity as it migrates toward throat forms, whereas limestone, influenced by complex pore structures and wettability conditions, shows more pronounced enrichment of adsorbed residual oil (12.2% corner adsorbed and 16.7% pore lining). Fundamentally, these differences stem from the multi-scale pore networks and strong oil-wet tendencies of carbonate rocks, where capillary forces act as the dominant resistance during displacement. Consequently, injected water preferentially channels through dominant flow paths, leaving small pores uncontacted while forming stable oil films in larger pores due to adsorption effects. As a result, residual oil in carbonate reservoirs is not only morphologically diverse but also exhibits extremely heterogeneous distribution, highlighting the urgent need for enhanced oil recovery technologies targeting wettability alteration and interfacial tension reduction.

4.3.4. *Effect of displacement velocity on microscopic residual oil*

In practical oilfield development, scientifically increasing the water injection rate can rapidly replenish reservoir energy,

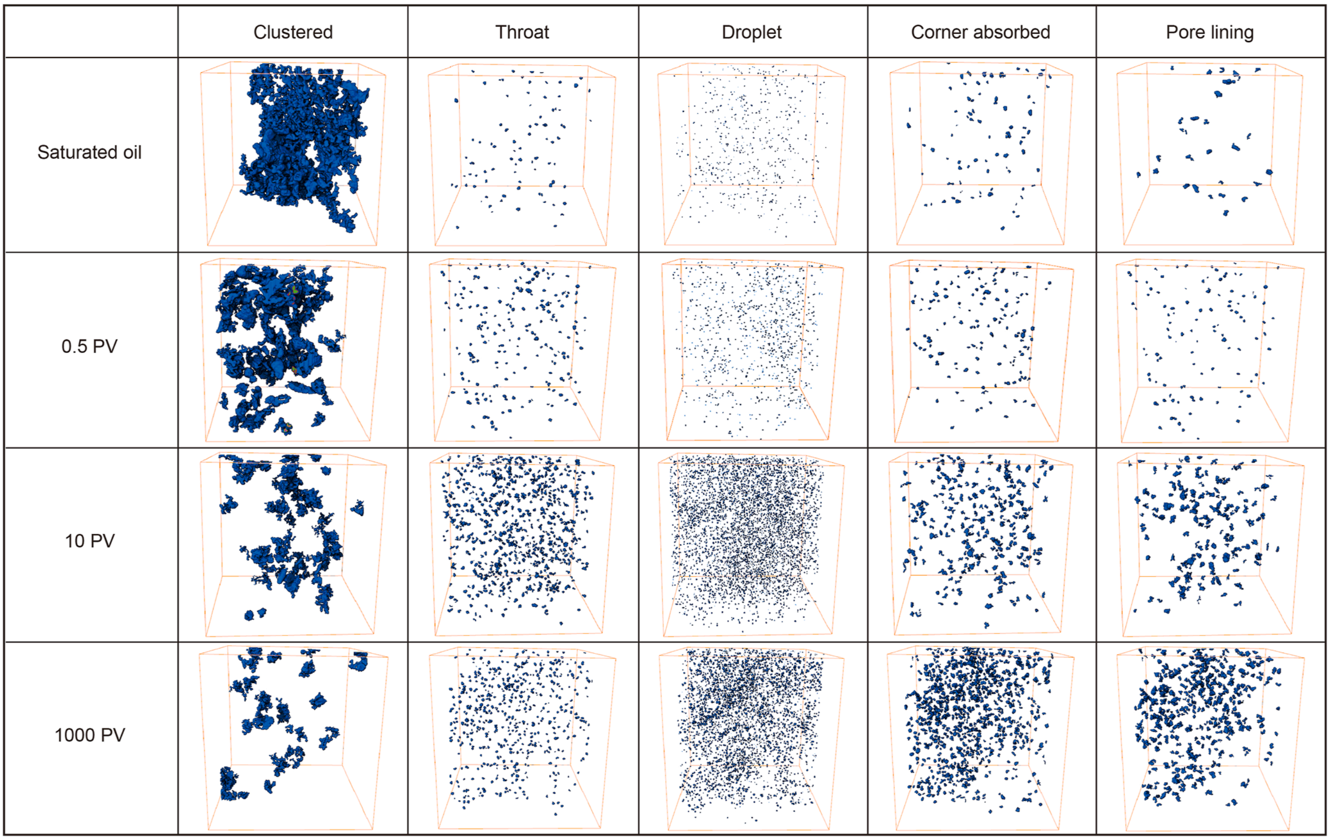

Fig. 10. Visualization of residual oil in limestone core (core 4) during LTWF.

Table 7
Summary of different types of microscopic residual oil (0.03 mL/min).

Core No.	Displacement stage	Residual oil type									
		Clustered		Throat		Droplet		Corner adsorbed		Pore lining	
		Oil saturation, %	Relative content, %	Oil saturation, %	Relative content, %	Oil saturation, %	Relative content, %	Oil saturation, %	Relative content, %	Oil saturation, %	Relative content, %
1	Saturated oil	59.1	80.3	3.9	5.3	2.6	3.6	4.1	5.6	3.8	5.2
	0.5 PV	51.7	75.8	4.0	5.8	3.3	4.8	4.3	6.3	4.9	7.3
	10 PV	43.6	68.6	4.4	6.9	4.2	6.6	4.6	7.2	6.8	10.7
	1000 PV	31.7	55.3	5.3	9.2	5.5	9.6	6.1	10.7	8.7	15.2
4	Saturated oil	61.3	78.1	4.9	6.3	4.5	5.8	3.4	4.3	4.3	5.5
	0.5 PV	46.6	72.8	4.8	7.5	4.0	6.3	4.1	6.4	4.6	7.2
	10 PV	36.5	60.2	5.0	8.3	4.9	8.1	6.5	10.8	7.6	12.6
	1000 PV	27.9	52.8	4.9	9.3	4.7	9.0	6.4	12.2	8.8	16.7

maintain or restore reservoir pressure, and thus provide a strong driving force for oil displacement, effectively stabilizing well productivity and mitigating production decline. Within a reasonable range, a higher injection rate also improves macroscopic sweep efficiency by promoting a more uniform advancement of the waterflood front, thereby displacing more oil. To investigate the impact of elevated injection rates on enhancing oil recovery in complex lithology carbonate reservoirs under high water injection volume, and to elucidate the mechanisms by which injection rate affects the distribution of various types of residual oil, the displacement rate in this study was increased from 0.03 to 0.3 mL/min. Subsequent CT scanning and residual oil analysis were performed, with Table 8 presenting the variations in microscopic residual oil content for dolomite and limestone under different flooding stages at a water injection rate of 0.3 mL/min.

To visualize the influence of injection rate on residual oil distribution in dolomite and limestone, the data from Tables 7 and 8 were integrated and plotted as shown in Fig. 11, illustrating the variation of microscopic residual oil under different displacement rates. The results indicate that, overall, increasing the displacement rate from 0.03 to 0.3 mL/min significantly enhances the utilization of macroscopic movable oil in the early stages of flooding (0.5 PV), particularly by improving the detachment and displacement of clustered and throat residual oil in both dolomite and limestone. Under low-rate flooding, clustered residual oil in dolomite and limestone accounted for over 78% in the saturated stage, decreasing only to 75.8% and 72.6% at 0.5 PV, respectively,

Table 8
Summary of different types of microscopic residual oil (0.3 mL/min).

Core No.	Displacement stage	Residual oil type									
		Clustered		Throat		Droplet		Corner adsorbed		Pore lining	
		Oil saturation, %	Relative content, %	Oil saturation, %	Relative content, %	Oil saturation, %	Relative content, %	Oil saturation, %	Relative content, %	Oil saturation, %	Relative content, %
1	Saturated oil	58.9	79.6	4.6	6.2	2.8	3.8	3.5	4.8	4.1	5.6
	0.5 PV	46.6	72.8	4.0	6.2	4.5	4.5	4.5	7.1	6.0	9.4
	10 PV	37.7	64.4	4.6	7.9	5.4	5.8	5.4	9.2	7.4	12.7
	1000 PV	27.9	52.5	5.2	9.8	6.7	7.2	6.7	12.6	9.5	17.9
4	Saturated oil	58.9	75.6	5.0	6.5	4.7	6.1	4.0	5.2	5.1	6.6
	0.5 PV	43.1	69.7	4.8	7.8	4.2	6.8	4.4	7.2	5.2	8.5
	10 PV	32.2	55.3	5.3	9.1	4.4	7.6	7.4	12.7	8.9	15.3
	1000 PV	22.5	48.3	4.9	10.5	4.1	8.8	6.3	13.6	8.7	18.8

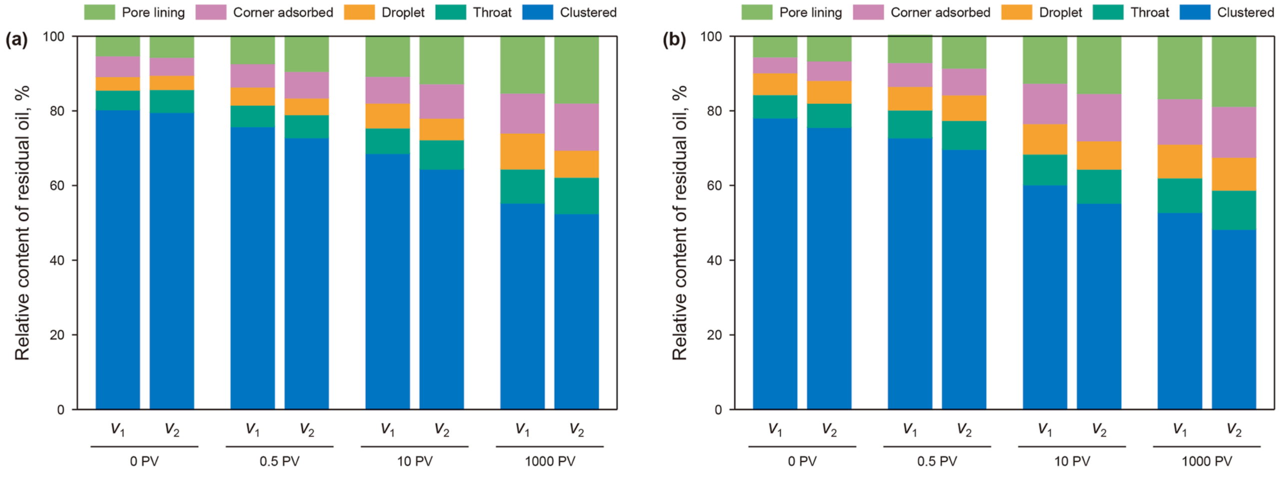

Fig. 11. Variation characteristics of different types of remaining oil ($v_1 = 0.03$ mL/min, $v_2 = 0.3$ mL/min). (**a**) Core 1 (dolomite); (**b**) core 4 (limestone).

indicating that waterflooding primarily advances along dominant channels without effectively utilizing large oil clusters within the pore space. Under high-rate flooding, however, clustered residual oil decreased to 72.8% in dolomite and 69.7% in limestone at 0.5 PV, an improvement of nearly 3%, suggesting that a higher displacement rate increased the pressure gradient at the flood front, effectively overcoming capillary forces restraining oil in large pores and facilitating earlier utilization of clustered residual oil. Nevertheless, as flooding progressed to 10 and 1000 PV, the decline of clustered residual oil slowed under high-rate flooding, with 52.5% and 48.3% of clustered residual oil remaining in dolomite and limestone at 1000 PV, respectively, reflecting persistent bypassed oil in matrix-deep regions due to strong heterogeneity and dual fracture-pore structures in carbonate reservoirs. Throat residual oil also showed a greater reduction under high-rate flooding compared to low-rate flooding, indicating that higher injection rates enhanced shear forces in narrow throats, aiding in the breakdown of trapped oil. However, at 1000 PV, its residual content remained around 10%, demonstrating that this oil type is primarily governed by small pore-throat radii and capillary forces. In contrast, droplet, corner adsorbed, and pore lining residual oils exhibited distinct trends under high-rate flooding. While droplet residual oil showed some reduction, its overall decrease was less pronounced than clustered or throat residual oils, indicating its control by wettability rather than displacement pressure. Corner adsorbed and pore lining residual oils slightly increased in proportion in the late stage of high-rate flooding (> 10 PV), with pore lining residual oil increasing by approximately 2% compared to low-rate flooding. This suggests that high-rate flooding preferentially utilized oil from large pores and throats, resulting in oil redistribution into thin films along pore walls and corners—an observation consistent with the persistent micro-residual oil characteristics in late-stage, high-water-cut carbonate reservoir development. The cores used in this study were oil-wet, where capillary forces resist displacement and promote pore lining residual oil.

Based on these findings, targeted strategies are recommended to improve the recovery of different residual oil types. For clustered and throat residual oils, increasing the displacement pressure gradient and employing cyclic or pulsed water injection can further utilize oil in deep and blind-end pores. For droplet and corner adsorbed residual oils, wettability alteration techniques, such as injecting low-interfacial-tension surfactants or alkali-polymer systems, can reduce capillary trapping, facilitating droplet coalescence and flow. For pore lining residual oil, gas flooding, water-alternating-gas injection, or nanoparticle-assisted flooding can destabilize and detach oil films, thereby enhancing ultimate recovery. Consequently, while increasing displacement rate significantly improves early-stage utilization of residual oil in large pores, achieving efficient carbonate reservoir development necessitates coupling high-rate injection with chemical or hybrid EOR methods to comprehensively address various types of microscopic residual oil.

5. Conclusions

In this study, long-term water flooding experiments were conducted on natural cores (dolomite and limestone) from the A oilfield in Iraq using NMR and CT scanning techniques. The research revealed the microscopic pore-throat displacement characteristics and dynamic evolution of residual oil in complex lithologic carbonate reservoirs under LTWF. These findings provide theoretical support for enhancing oil recovery in complex lithologic carbonate reservoirs in the Middle East. The main conclusions are as follows:

(1) Limestone has better reservoir properties, and the recovery factor for limestone cores under LTWF is significantly higher than that of dolomite cores.
(2) Microscale micropores and microscale macropores in the core are the primary contributors to the recovery factor. As the displacement volume increases, the utilization degree of oil in submicron pores gradually increases, although oil in nanopores still cannot be produced.
(3) After LTWF, residual oil mainly resides in nanopores and submicron pores. Enhancing the producing of oil in these two pore types will be a key focus for improving recovery in subsequent complex lithology carbonate reservoirs.
(4) The dolomite exhibits poorer physical properties, and apart from clustered residual oil, the other four types of residual oil are relatively evenly distributed. The migration of residual oil in dolomite is primarily from clustered type to throat type, indicating poor continuity of residual oil. Therefore, the subsequent development of residual oil should focus on improving microscopic displacement efficiency.
(5) Limestone exhibits better physical properties, with a higher degree of transformation from clustered residual oil to other discontinuous types. Due to the predominantly oil-wet nature of carbonate rocks, capillary forces act as a resistance to oil displacement. As the water flooding pore volume increases, the proportion of adsorbed residual oil (corner adsorbed + pore lining) becomes significant. The development of this type of residual oil should primarily focus on enhancing displacement efficiency.

CRediT authorship contribution statement

Kai-Jun Tong: Resources, Methodology. **Yue Pan:** Writing – review & editing, Writing – original draft. **Sheng Guo:** Software, Methodology. **Xiao-Cong Lyu:** Writing – review & editing, Validation. **Han Chen:** Visualization, Data curation, Conceptualization. **Hui-Qing Liu:** Writing – review & editing, Supervision. **Zhi-Xue Sun:** Methodology, Formal analysis. **Jia-Wei Tang:** Software, Methodology.

Declaration of competing interest

The authors declare that they have no known competing financial interests or personal relationships that could have appeared to influence the work reported in this paper.

Acknowledgments

The authors gratefully acknowledge the financial support provide by the Major Science and Technology Project of CNOOC (grant No. KJGG2022-0905).

References

Benavides, F., Leiderman, R., Souza, A., Carneiro, G., Bagueira, R., 2017. Estimating the surface relaxivity as a function of pore size from NMR T_2 distributions and micro-tomographic images. Comput. Geosci. 106, 200–208. https://doi.org/10.1016/j.cageo.2017.06.016.

Bhicajee, P., Romero-Zerón, L., 2021. Effect of different low salinity flooding schemes and the addition of alkali on the performance of low-salinity waterflooding during the recovery of heavy oil from unconsolidated sandstone. Fuel 289, 119981. https://doi.org/10.1016/j.fuel.2020.119981.

Chai, R.K., Liu, Y.T., He, Y.T., Liu, Q.J., Xue, L., 2022. Dynamic behaviors and mechanisms of fluid-fluid interaction in low salinity waterflooding of carbonate reservoirs. J. Petrol. Sci. Eng. 208, 109256. https://doi.org/10.1016/j.petrol.2021.109256.

Darvish, S.A., Ayatollahi, S., Bahari, M.M., 2019. Smart water flooding performance in carbonate reservoirs: An experimental approach for tertiary oil recovery. J. Pet. Explor. Prod. Technol. 9, 2643–2657. https://doi.org/10.1007/s13202-019-0650-9.

Gao, H., Li, H.Z., 2015. Determination of movable fluid percentage and movable fluid porosity in ultra-low permeability sandstone using nuclear magnetic resonance (NMR) technique. J. Petrol. Sci. Eng. 133, 258–267. https://doi.org/10.1016/j.petrol.2015.06.017.

Gong, W.B., Liu, Y., Xi, C.D., Yang, G., Ju, Y., Wang, M.R., 2024. Dynamic characterization of residual oil during long-term waterflooding experiments in heterogeneous porous structures. Fuel 356, 129567. https://doi.org/10.1016/j.fuel.2023.129567.

Gong, Y.J., Liu, K.Y., 2020. Pore throat size distribution and oiliness of tight sands–A case study of the Southern Songliao Basin, China. J. Petrol. Sci. Eng. 184, 106508. https://doi.org/10.1016/j.petrol.2019.106508.

Han, S.C., Li, L.L., Hu, S., Jing, C.H., Wu, X.D., Yang, J.C., Liu, T., Xiao, C.Y., 2025. Experimental study of acid fracturing behavior in carbonate reservoirs with different fracture-cavity development. Pet. Sci. 22 (7), 2937–2949. https://doi.org/10.1016/j.petsci.2025.04.022.

Hu, Y.B., Guo, Y.H., Shangguan, J.W., Zhang, J.J., Song, Y., 2020. Fractal characteristics and model applicability for pores in tight gas sandstone reservoirs: A case study of the upper Paleozoic in Ordos Basin. Energy & Fuels 34 (12), 16059–16072. https://doi.org/10.1021/acs.energyfuels.0c03073.

Iraji, S., Almeida, T.R.D., Munoz, E.R., Basso, M., Vidal, A.C., 2024. The impact of heterogeneity and pore network characteristics on single and multi-phase fluid propagation in complex porous media: An X-ray computed tomography study. Pet. Sci. 21 (3), 1719–1738. https://doi.org/10.1016/j.petsci.2024.01.015.

Jafari, J., Mahboubi, A., Moussavi-Harami, R., Al-Aasm, I.S., 2020. The effects of diagenesis on the petrophysical and geochemical attributes of the Asmari Formation, Marun oil field, southwest Iran. Pet. Sci. 17, 292–316. https://doi.org/10.1007/s12182-019-00421-0.

Jia, P., Li, Y., Guo, H.X., Feng, H.R., Cheng, L.S., 2023. Experimental study of pore-scale water flooding with phase change based on a microfluidic model in volatile carbonate reservoirs. Appl. Sci. 13 (11), 6642. https://doi.org/10.3390/app13116642.

Joudaki, M., Baghbani, D., 2018. Biostratigraphy of Oligocene and lower Miocene deposits, Anneh Anticline, folded Zagros, SW of Iran. Carbonates Evaporites 33 (3), 509–515. https://doi.org/10.1007/s13146-017-0362-5.

Khazaie, E., Noorian, Y., Kavianpour, M., Mousavi-Harami, R., Mahboubi, A., Omidpour, A., 2022. Sedimentological and diagenetic impacts on porosity systems and reservoir heterogeneities of the Oligo-Miocene mixed siliciclastic and carbonate Asmari reservoir in the Mansuri oilfield, SW Iran. J. Petrol. Sci. Eng. 213, 110435. https://doi.org/10.1016/j.petrol.2022.110435.

Li, F., Hou, J., Qiu, M.X., Meng, X.H., Zhang, Y.H., Zhou, K., 2012. CT experiments and image processing for the water-oil displacement at pore scale. Procedia Eng. 29, 3831–3835. https://doi.org/10.1016/j.proeng.2012.01.579.

Li, J.J., Jiang, H.Q., Wang, C., Zhao, Y.Y., Gao, Y.J., Pei, Y.L., Wang, C.C., Dong, H., 2017. Pore-scale investigation of microscopic remaining oil variation characteristics in water-wet sandstone using CT scanning. J. Nat. Gas Sci. Eng. 48, 36–45. https://doi.org/10.1016/j.jngse.2017.04.003.

Li, J.J., Gao, Y.J., Jiang, H.Q., Liu, Y., Dong, H., 2018. Pore-scale imaging of the oil cluster dynamic during drainage and imbibition using in situ X-ray microtomography. Geofluids 2018, 7679607. https://doi.org/10.1155/2018/7679607.

Li, S.Q., Liu, Y.T., Xue, L., Yang, L., Yuan, Z.W., Jian, C.S., 2021. An investigation on water flooding performance and pattern of porous carbonate reservoirs with bottom water. J. Petrol. Sci. Eng. 200, 108353. https://doi.org/10.1016/j.petrol.2021.108353.

Li, Z.F., Su, Y.L., Li, L., Hao, Y.M., Wang, W.D., Meng, Y., Zhao, A., 2022. Evaluation of CO_2 storage of water alternating gas flooding using experimental and numerical simulation methods. Fuel 311, 122489. https://doi.org/10.1016/j.fuel.2021.122489.

Liu, J.L., Xie, R.H., Guo, J.F., Jin, G.W., 2025. Numerical investigation on 2-D NMR response mechanisms and the frequency conversion of petrophysical parameters in shale oil reservoirs. Pet. Sci. 22 (5), 1959–1976. https://doi.org/10.1016/j.petsci.2025.03.014.

Liu, X.F., Wang, J.F., Ge, L., Hu, F.L., Li, C.L., Li, X., Yu, J., Xu, H.J., Lu, S.F., Xue, Q.Z., 2017. Pore-scale characterization of tight sandstone in Yanchang formation Ordos Basin China using micro-CT and SEM imaging from nm- to cm-scale. Fuel 209, 254–264. https://doi.org/10.1016/j.fuel.2017.07.068.

Liu, Y.G., Jia, P., Tong, K.J., 2023. Pore-scale experimental investigation of the residual oil formation in carbonate sample from the Middle East. Processes 11 (8), 2289. https://doi.org/10.3390/pr11082289.

Mansi, M., Mehana, M., Fahes, M., Viswanathan, H., 2020. Thermodynamic modeling of the temperature impact on low-salinity waterflooding performance in sandstones. Colloids Surf. A Physicochem. Eng. Asp. 586, 124207. https://doi.org/10.1016/j.colsurfa.2019.124207.

McLendon, W.J., Koronaios, P., Enick, R.M., Biesmans, G., Salazar, L., Miller, A., Soong, Y., McLendon, T., Romanov, V., Crandall, D., 2014. Assessment of CO_2-soluble non-ionic surfactants for mobility reduction using mobility measurements and CT imaging. J. Petrol. Sci. Eng. 119, 196–209. https://doi.org/10.1016/j.petrol.2014.05.010.

Mostaghimi, P., Blunt, M.J., Bijeljic, B., 2013. Computations of absolute permeability on micro-CT images. Math. Geosci. 45, 103–125. https://doi.org/10.1007/s11004-012-9431-4.

Pan, Y., Liu, H.Q., Tang, J.W., Zhou, S., Luo, C., Wang, Z.C., Liu, R.J., Chen, P.Y., 2024. Experimental study on carbonated water flooding enhanced volatile reservoirs recovery based on NMR technology. In: SPE Abu Dhabi International Petroleum Exhibition and Conference. https://doi.org/10.2118/222824-MS.

Qin, X.J., Xia, Y.X., Wu, J.S., Sun, C.H., Zeng, J.H., Xu, K., Cai, J.C., 2022. Influence of pore morphology on permeability through digital rock modeling: New insights from the Euler number and shape factor. Energy & Fuels 36 (14), 7519–7530. https://doi.org/10.1021/acs.energyfuels.2c01359.

Sadeghi, R., Vaziri-Moghaddam, H., Taheri, A., 2011. Microfacies and sedimentary environment of the Oligocene sequence (Asmari Formation) in Fars sub-basin, Zagros Mountains, southwest Iran. Facies 57, 431–446. https://doi.org/10.1007/s10347-010-0245-x.

Sagbana, P.I., Sarkodie, K., Nkrumah, W.A., 2023. A critical review of carbonate reservoir wettability modification during low salinity waterflooding. Petroleum 9 (3), 317–330. https://doi.org/10.1016/j.petlm.2022.01.006.

She, Y., Zhang, C.W., Mahardika, M.A., Patmonoaji, A., Hu, Y.X., Matsushita, S., Suekane, T., 2021. Pore-scale study of in-situ surfactant flooding with strong oil emulsification in sandstone based on X-ray microtomography. J. Petrol. Sci. Eng. 98, 247–261. https://doi.org/10.1016/j.jiec.2021.03.046.

Snosy, M.F., Abu, E.E.M., El-Banbi, A., Sayyouh, H., 2022. Comprehensive investigation of low salinity waterflooding in carbonate reservoirs. J. Pet. Explor. Prod. Technol. 12, 701–724. https://doi.org/10.1007/s13202-021-01330-y.

Song, F.Q., Ji, K., Bo, L.W., 2018. The mathematical model of water flooding in different structure types of low permeability carbonate rocks. IOP Conf. Ser. Earth Environ. Sci. 186 (3), 012003. https://doi.org/10.1088/1755-1315/186/3/012003.

Song, X.M., Li, Y., 2018. Optimum development options and strategies for water injection development of carbonate reservoirs in the Middle East. Petrol. Explor. Dev. 45 (4), 723–734. https://doi.org/10.1016/S1876-3804(18)30075-2.

Tang, H., Jia, C., Lu, H., Deng, Y., Zhu, B., 2024. Numerical simulation of residual oil distribution characteristic of carbonate reservoir after water flooding. Front. Earth Sci. 12, 1395483. https://doi.org/10.3389/feart.2024.1395483.

Tong, K.J., He, J., Chen, P.Y., Li, C.Y., Dai, W.H., Sun, F.T., Tong, Y., Rao, S., Wang, J., 2024. Key technologies for the efficient development of thick and complex carbonate reservoirs in the Middle East. Energies 17 (18), 4566. https://doi.org/10.3390/en17184566.

Wang, F.J., Wang, X., Liu, Y.K., Deng, Q.J., Xu, J.J., Zhang, Y., Li, H.Y., 2021. The evolutionary characteristics of reservoir microstructure under long-term waterflooding development and its fractal description. Geofluids 2021, 5557125. https://doi.org/10.1155/2021/5557125.

Wang, H.M., Zhou, Q., Sheng, J.C., Luo, Y.L., Liu, J., Liu, X.X., 2023. Effect of long-term infiltration on porosity-permeability evolution in carbonate rocks: An online NMR coupling penetration test. J. Hydrol. 617, 129029. https://doi.org/10.1016/j.jhydrol.2022.129029.

Wang, L.H., Li, X.F., Wang, J.L., Zhang, H.B., Shi, H.G., Liu, G.F., Yang, D.Y., 2025. Effect of pore-throat structure on irreducible water saturation and gas seepage capacity in a multilayer tight sandstone gas reservoir. Geoenergy Sci. Eng. 249, 213787. https://doi.org/10.1016/j.geoen.2025.213787.

Washburn, K.E., Sandor, M., Cheng, Y.S., 2017. Evaluation of sandstone surface relaxivity using laser-induced breakdown spectroscopy. J. Magn. Reson. 275, 80–89. https://doi.org/10.1016/j.jmr.2016.12.004.

Yang, Y., Liao, G.Z., Xiong, W., Shen, R., Zhang, J., Li, Q., Wang, S.Z., Zhang, J.Z., Tan, L.F., Shao, G.Y., 2022. Physical and numerical simulation of inter-fracture flooding in heterogeneous tight oil reservoirs. Energy Rep. 8, 12970–12978. https://doi.org/10.1016/j.egyr.2022.09.194.

Zhang, Z.C., Bai, M.X., Du, S.Y., 2024. Characteristics of pore dynamics in shale reservoirs by CO_2 flooding. Petrol. Res. Eval. Develop. 14 (1), 42–47. https://doi.org/10.13809/j.cnki.cn32-1825/te.2024.01.006 (in Chinese).